Digital Imaging Fluorescence Microscopy: Spatial Heterogeneity of Photobleaching Rate Constants in Individual Cells

DOUGLAS M. BENSON, JOSEPH BRYAN, ANNE L. PLANT, ANTONIO M. GOTTO, JR., and LOUIS C. SMITH

Departments of Medicine and Cell Biology, Baylor College of Medicine and The Methodist Hospital, Houston, Texas 77030

ABSTRACT Photobleaching and related photochemical processes are recognized experimental barriers to quantification of fluorescence by microscopy. We have measured the kinetics of photobleaching of fluorophores in living and fixed cells and in microemulsions, and have demonstrated the spatial variability of these processes within individual cells. An inverted fluorescence microscope and a high-sensitivity camera, together with high-speed data acquisition by a computer-controlled image processor, have been used to control precisely exposure time to excitation light and to record images. To improve the signal-to-noise ratio, 32 digital images were integrated. After correction for spatial variations in camera sensitivity and background fluorescence, the images of the relative fluorescence intensities for 0.065 μm^2 areas in the object plane were obtained.

To evaluate photobleaching objectively, an algorithm was developed to fit a three-parameter exponential equation to 20 images recorded from the same microscope field as a function of illumination time. The results of this analysis demonstrated that the photobleaching process followed first-order reaction kinetics with rate constants that were spatially heterogeneous and varied, within the same cell, between 2- and 65-fold, depending on the fluorophore. The photobleaching rate constants increased proportionally with increasing excitation intensity and, for benzo(a)pyrene, were independent of probe concentration over three orders of magnitude (1.25 μM to 1.25 mM). The propensity to photobleach was different with each fluorophore. Under the cellular conditions used in these studies, the average rates of photobleaching decreased in this order: *N*-(7-nitrobenz-2-oxa-1,3-diazole)-23,24-*dinor*-5-cholen-22-amine-3β-ol > acridine orange > rhodamine-123 > benzo(a)pyrene > fluorescein > tetramethylrhodamine > 1,1'dioctadecyl-3,3,3',3'-tetramethylindocarbocyanine. The photobleaching appears to be an oxidation reaction, in that the addition of saturated solutions of $Na_2S_2O_5$ to mineral oil microemulsions eliminated photobleaching of *N*-(7-nitrobenz-2-oxa-1,3-diazole)-23,24-*dinor*-5-cholen-22-amine-3β-ol or benzo(a)pyrene. We identified experimental conditions to observe, without detectable photobleaching, fluorophores in living cells, which can not be studied anaerobically. Useful images were obtained when excitation light was reduced to eliminate photobleaching, as determined from zero-time images calculated from the exponential fit routine. The results show that, with conventional illumination and photographic methods, the fluorescence of regions with high rate constants for photobleaching are significantly underrepresented, and can be as much as 20-fold.

Fluorescence microscopy is an attractive method to study the dynamics of various cellular processes and to elucidate the internal architecture of individual cells that uses appropriately labeled fluorescent antibodies and proteins. Work by a large

number of laboratories has been directed, for example, at detailing the localization of actin, tubulin, and intermediate filament proteins and various molecules that associate with these fibers. The selective uptake and localization of intracellular fluorescent compounds have been used to identify specific intracellular structures. For example, lysosomes are visualized by acridine orange (1), mitochondria by rhodamine-123 (2), and DNA by propidium iodide (3) or benzamidine dyes such as Hoechst 33258 (4, 5). By using low light level video cameras, dynamic processes such as the internalization of fluorescently labeled ligands by receptors (6) or the redistribution of microinjected proteins (7) have been observed in living cells. In most of these studies, the fluorescence intensity has been used as a subjective measure of the spatial distribution of the fluorophores. A general dictum has been that quantification was at best difficult or, at worst, impossible (8, 9). A number of quantitative studies have been undertaken to measure various intracellular metabolic states (10–13), oxygen (14, 15), pH (16, 17), and various kinetic processes such as diffusion coefficients of fluorescent molecules (18–21). In general, these measurements have been restricted to and integrated over a small area of the microscope field, with little effort to retain spatial information. A number of recent efforts that use low light level cameras and video digital image processing devices have been directed at obtaining quantitative information on the spatial, spectral, and radiometric distribution of fluorophores within single cells (14, 17, 22–28). Benson et al. (14) have demonstrated that an image processor incorporated into a video-intensified microscopy system can provide a quantitative measure of the spatial distribution of the fluorescence intensity and can be used to determine oxygen concentration by fluorescence quenching.

One major complication in all of the quantitative work that has not been evaluated systematically is photobleaching of the fluorophores. This photochemical process produces a loss of fluorescence intensity during intermittent or constant illumination. The high numerical aperture objectives currently in use, which maximize spatial resolution and improve the limits of detection, simultaneously accelerate photobleaching, inasmuch as the incident illumination system projects the excitation light through the objective into a small area of the microscope field, increasing the light intensity by at least a factor of 1,000- to 10,000-fold. This factor is calculated from the ratio of the area of the collector lens of the excitation lamp housing to that of the illuminated area in the object plane.

In this article, we describe a digital imaging microscopy system to study dynamic processes requiring radiometric, spatial, and spectral information about several fluorophores. We have used this system to investigate the mechanism and consequences of photochemical reactions and the intracellular variability of these processes. First, we demonstrate the spatial heterogeneity of photobleaching rates of several commonly used fluorophores. Second, we describe analytic procedures to establish objectively the rate of photobleaching and to make corrections for photobleaching. Finally, we identify experimental conditions to observe, without detectable photobleaching, kinetic processes involving fluorophores in living cells.

MATERIALS AND METHODS

Instrumentation: The microscope used in the system, shown schematically in Fig. 1, is a Leitz Diavert (E. Leitz, Inc., Rockleigh, NJ) equipped with a Ploempak epi-illuminator, a 100-W Hg arc, a long working-distance condenser, and a 100-W quartz-halogen source for transmitted light. Electronic shutters for both the incident and transmitted light sources, an X–Y scanning stage (5-μm steps), a stepping motor for focus control (0.1-μm steps), and a solenoid-activated neutral density filter bank (MTS, Inc., Houston, TX) for step attenuation in excitation flux, have been added and controlled by an LSI 11/23 microcomputer (Data Translation, Inc., Marlboro, MA). The image from the microscope was projected on a silicon-intensified target video camera (Hamamatsu Corp., Middlesex, NJ, model C1000-12). Using a × 63, 1.4 numerical aperture (NA) objective and a 40-mm extension tube, an area, 128 × 111 μm, of the sample field was projected onto the 12.7 × 11.0-mm area of the active surface of the intensification target. The analog output from the camera was fed simultaneously to both a time-date generator and to a high-speed analog/digital (A/D) converter in a Grinnell image processor (model 274) (Grinnell Systems Corp., San Jose, CA).

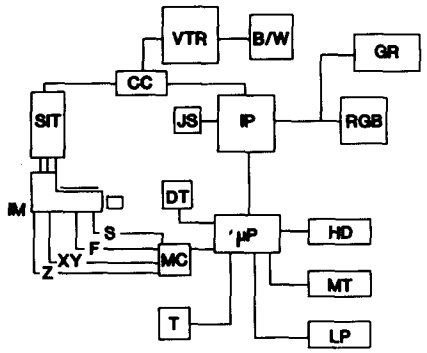

FIGURE 1 Schematic of digital imaging system. *IM*, Inverted microscope; *SIT*, silicon-intensified video camera; *CC*, camera control; *VTR*, time-lapse video tape recorder; *B/W*, black and white monitor; *IP*, digital image processor; *JS*, joystick; *RBG*, high-resolution color monitor; *GR*, graphics recorder with 35-mm camera; *μp*, LSI 11/23 computer; *DT*, digitizing tablet; *HD*, 20 Mbyte Winchester disk; *MT*, magnetic tape; *LP*, line printer; *MC*, microscope controller with interfaces to the shutters (*S*), neutral-density filters (*F*), stage positioner (*X*, *Y*), and focus (*Z*). Details are found in Materials and Methods.

The image processor can store three images consisting of 512 × 480 arrays of picture elements or pixels. The A/D converter quantizes the analog intensity at each pixel to a value between 0 and 255, or 8 bits. The images can be displayed in either black and white or pseudo-color. The output from all three-image channels were either displayed as a full-color composite on a high-resolution red/green/blue monitor or used to compare three individual images in different colors. Images were photographed on 35-mm film by a Matrix 3000 color graphic recorder (Matrix, Inc., Mesa, AZ). The image processor was also interfaced to the LSI 11/23 with 256,000 bytes random access memory, dual 1 Mbyte floppy disks, and 20 Mbyte Winchester disk (Charles River Data Systems, Inc., Framingham, MA) for program and image storage, and a Cipher model F880 streaming magnetic tape drive (Cipher Data Products, San Diego, CA) for archiving images.

Image Acquisition, Processing, and Analysis: A software package written in Fortran operating under RT-11 (Digital Equipment Corp., Marlboro, MA) was developed to focus the microscope, to control the stage position, and to synchronize the opening of the excitation shutters with the sampling interval of the image processor. Although the image processor digitized and stored frames internally at 30 Hz, 5 s was required to transfer a full image, 245, 760 bytes, to the disk storage device. An improvement in transfer rate could be obtained by reducing the sample size. A maximum sampling rate of 15 Hz was achieved for a single pixel. Phase and fluorescence images were acquired and stored automatically at selected time intervals as indicated.

A number of image processing routines have been developed, including subtraction to remove background and dark current contributions, division to correct for camera shading, and feature or area selection using an overlay mask. Other available enhancement routines include contrast stretching, histogram equalization, pseudo coloring, and spatial derivatives. These routines can be performed at video rates and are interactive with either the joystick or a digitizing tablet. The intensity distribution of the images or subsampled features within a field can be analyzed to determine the mean, standard deviation, range, and integrated intensities of the selected areas. A program was written to display data as a bivariate frequency histogram (29), as indicated in the figure legends. The displayed areas had pixel frequences ≥5. For the isometric plots (30), the data set for each column was rotated 45° with respect to the *x*-

axis and, for each row, was rotated 15° with respect to the y-axis, and the pixel value was projected along the z-axis with an algorithm for removing hidden lines. For the difference plots, to avoid wrap around of negative values on the display, all values were offset by 128. Where indicated, images were convolved with a low pass filter (3 by 3 unity matrix) (29).

To determine rates of photobleaching objectively, images were analyzed using a nonlinear least squares fit of a three-parameter exponential (31) that was modified to calculate the parameters and associated errors for an entire image on a pixel-by-pixel basis. The equation is

$$I_{(x,y,t)} = A_{(x,y)} + B_{(x,y)}\exp(-k_{(x,y)}t),$$

where $I_{(x,y,t)}$ is fluorescence intensity at pixel $_{(x,y)}$ at time t; $A_{(x,y)}$ is fluorescence intensity at $t = \infty$; $A_{(x,y)} + B_{(x,y)}$ is the fluorescence intensity at $t = 0$; and $k_{(x,y)}$ is the rate constant for the intensity change at pixel (x,y). For a routine calculation, 20 images, one per time point, were used to determine the values for these parameters.

Estimation of the errors in photographic recording of fluorescence that photobleaches involved comparison of the calculated initial intensity values at zero time with the residual intensity values obtained by summation of the 20 images acquired during the photobleaching experiments. The reasoning is that photographic recording would integrate the decreasing intensities for about the same time used to determine the photobleaching rates. The difference between the zero-time image and the summed image or "photograph" was obtained by two difference calculations, which gave the same result. The first calculation involves summation of 20 zero-time images, which would be produced if there were no photobleaching. Subtraction of the "photograph" from this summed zero-time image produced the difference image due to photobleaching. Alternatively, the intensity values obtained by summation of the photobleaching images were divided by 20, the number of images acquired over the time course of the experiment, to obtained the "photograph" which was subtracted from the zero-time image.

Multiple fluorophores were excited with three standard filter cubes provided by Leitz. The spectral bands isolated by these cubes were (*a*) excitation wavelength centered at 365 nm with half band width of 45 nm and emission at wavelengths >418 nm for cube A; (*b*) excitation wavelength centered at 480 nm with half band width of 10 nm and emission at wavelengths >515 nm for cube I2; and (*c*) excitation wavelength centered at 545 nm with half band width of 33 nm and emission at wavelengths >577 nm for the N cube. A series of solenoid switches were used to position three neutral-density filters in the excitation light path, as desired. Combinations of these filters provided reproducible attenuation of the excitation intensity from 40 to 0.4%. Fluorescence standards of either 1 μM anthracene or 3 μM rhodamine B embedded in polymethylmethacrylate (Starna Cells Inc., Atascadero, CA) served as photostable references to monitor day-to-day variation in the excitation source. A 100-W Hg arc lamp was used for no >100 h total, after which the decreased stability and output made it unusable.

Cell Cultures and Labeling Procedures: Human foreskin fibroblasts (7–11th passage) were cultured on sterilized 50-mm² No. 1 coverslips with Dulbecco's modified eagle's medium supplemented with 10% fetal calf serum, streptomycin (50 μg·ml^{-1}), penicillin (50 μg·ml^{-1}), and 1 mM glutamine.

Benzo(a)pyrene was obtained from Aldrich and purified by high performance chromatography on reverse-phase octadecyl-silica in 80% acetonitrile (32). Low density lipoproteins (LDL)[1] were prepared and labeled with benzo(a)pyrene as described by Plant et al. (32). The lipid content of fibroblasts was increased by incubation with LDL at 200 μg of lipoprotein protein·ml^{-1} for 24 h. Cells were labeled with benzo(a)pyrene by incubation with LDL-benzo(a)pyrene at 50 μg of lipoprotein protein·ml^{-1} for 1 h.

N-(7-nitrobenz-2-oxa-1,3-diazole)-23,24-*dinor*-5-cholen-22-amine-3β-ol (NBD-cholesterol) was prepared as previously described (33). NBD-cholesterol, 30 mol%, was incorporated into 1-palmitoyl-2-oleoyl-phosphatidylcholine vesicles and mixed in media containing lipoprotein-deficient serum at a final fluorophore concentration of 10 μM. This solution was added to plates of fibroblasts at a plating density of 10^6 cells per 100-mm dish and allowed to incubate for 24 h at 37°C.

Benzo(a)pyrene was also incorporated into micromolecules of mineral oil for model studies. Benzo(a)pyrene concentrations ranging from 0.125 μM to 1.25 mM in mineral oil were added to 4 vols of distilled H_2O containing 4 mg·ml^{-1} of Na deoxycholate to stabilize the emulsion. All measurements of benzo(a)pyrene fluorescence were made with the cube A filter set.

Primary cultures of rat hepatocytes plated on 50 × 50-mm No. 1 coverslips were a gift of Dr. Bette C. Sherrill, Department of Medicine. After 72 h in culture, cells were labeled with 5 μg·ml^{-1} acridine orange in media for 10 min, and then washed three times with fresh media. Cells on coverslips were transferred to a teflon chamber (Bionique, Corning, Lake Placid, NY) with a sealed cover to provide a controlled environment for viewing living cells on the microscope. Ports in the chamber top permitted rapid change of media and substrates and the constant flow of a humidified mixture of 5% CO_2 in air. The stage and chamber temperature was maintained at 37°C with two heated blowers and monitored with a microprobe (Bailey Instrument Co., Inc., Saddle Brook, NJ) in the chamber. Cells have remained viable for as long as 16 h before significant evaporation of the media. The chamber volume was 2 ml.

[1] *Abbreviations used in this paper:* FITC, fluorescein isothiocyanate; LDL, low density lipoproteins; NBD-cholesterol, *N*-(7-nitrobenz-2-oxa-1,3-diazole)-23,24-*dinor*-5-cholen-22-amine-3β-ol.

RESULTS

The silicon-intensified target video camera was tested monthly for linearity and spatial resolution using a Mini-Optoliner projector (Optical Instruments Corp., Buena Park, CA) with a calibrated radiometric and spatial response. This instrument has a 2,800 °K, 6-V tungsten source that was used to project 3.5×10^{-7} lm·cm^{-2} directly onto the detector faceplate. By attenuating the light with the appropriate quartz neutral-density filters, the camera was found to be linear between 0.033 and 1.2 nW·cm^{-2} (Fig. 2, top). With maximum gain of

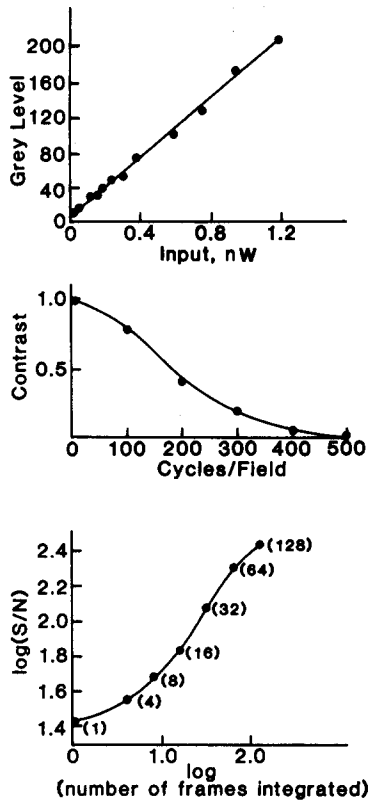

FIGURE 2 Camera response and system noise characteristics. (*Top*) Camera linearity. The input light intensity was varied from 0.033 to 1.2 nW cm^{-2} with the appropriate spectrophotometrically calibrated quartz neutral-density filters (Corion). The output intensity was determined from the mean field intensity after subtraction of the camera dark current and normalization of the shading effects of the camera. (*Center*) Contrast transfer function. As described in the text, the contrast measured in the center of the field was corrected for the modulation transfer function of the projector. (*Bottom*) Signal-to-noise ratio as a function of the number of frames integrated. The noise was measured as the standard deviation, on a pixel-by-pixel basis for 61,440 pixels, calculated from eight replicate samples for the indicated number of frames integrated. The signal-to-noise ratio was calculated from the slope of the regression of the standard deviation versus the mean for each pixel at a given integration number.

the camera controller, an incident flux of 1.2 $nW \cdot cm^{-2}$, integrated between 380 and 700 nm, gave a mean intensity response equivalent to 200 of the 255 grayscales detected by the camera.

Variation in pixel response was measured by projecting a flat, homogeneous field (<8% variation) onto the camera target. At this intensity, the camera gave a mean field grayscale of 200, and a range of pixel values between 160 and 233, ~36% variation. This spatial variation in sensitivity of the detector was eliminated by applying a shading correction derived as follows (34). A "mask" image, $M_{(x,y)}$, was generated using a flat, uniformly fluorescent object. Routinely, the polymethacrylate Starna cells, which are sold as fluorescent standards for conventional fluorimetry, were used. Neutral-density filters were selected to bring the mean pixel intensity to a gray scale value of 200. The mask image was then digitized and stored. The experimental image was then acquired and divided, on a pixel-by-pixel basis, by the mask. Each pixel was then multiplied by 200 to generate the corrected output image. Formally, the operation is

$$\text{Image}_{\text{out}_{(x,y)}} = \frac{\text{Image}_{\text{in}_{(x,y)}}}{\text{Mask}_{(x,y)}} \times 200.$$

When this operation was performed using a second sample of the fluorescent standards as an input image, the output images were uniformly linear over the entire field with a coefficient of variation of ~2%. In that the shading was due to contributions from the camera electronics and the focus of the excitation light, a correction mask was stored for each of the filter combinations.

The effective resolution of the camera, which determines the smallest sampling area (29), was measured using a test target in the Optoliner. This test target has vertical opaque lines ruled at varying spatial frequencies. The target was projected and digitized to determine the maximum and minimum intensities at a given spatial frequency. The difference between these intensities is defined by the maximum contrast difference on the target to give a contrast-transfer function (29), described as

$$C = \frac{I_p - I_v}{I_o - I},$$

where I_p and I_v are the peak and valley intensities for a given frequency (line pairs per picture width) versus the intensities of a maximum contrast, white (I_o) and black (I), area. Fig. 2 (center) shows the contrast-transfer function for the Hamamatsu silicon-intensified target camera. A 40% contrast was observed at 200 line pairs/field. As expected, the contrast decreased radially from the optical axis, with a contrast of 33% at the corners of the detector.

To reduce the signal-to-noise ratio, sequential frames were integrated (35). Because the transfer time for each image from the image processor to the computer required 4–5 s, frame integration was performed in the image processor at video rates (30 Hz) by summing 2^n frames in a 16-bit frame buffer (two-image channels), dividing by the appropriate power of 2, and truncating to 8 bits. These images were then transferred and stored for subsequent analysis. An image of the defocused edge of the prism in the binocular element of the microscope was used for analysis of the signal-to-noise ratio. Stored images with varying numbers of integrated frames were averaged by the computer with 32-bit precision to determine the mean intensity and standard deviation on a pixel-by-pixel basis. For the single and for the four-frame integration, 20 stored images were averaged. For the 8-, 16-, 32-, 64-, and 128 frame integration, eight stored images were averaged. A bivariate frequency histogram was used to analyze the correlation between the standard deviation and the mean intensity values for integrated frame images. The signal-to-noise was calculated from the slope of the regression of these points. Fig. 2 (bottom) illustrates the signal-to-noise as a function of the number of frames integrated. A 32-frame integration in the image processor required a 1.07-s exposure, total elapsed time. If 32 single frames had been acquired individually for subsequent averaging in the computer, the exposure time would have been 6.4 s, with a total elapsed time of 160 s. The 32-frame integration was used as a compromise between increased photobleaching at longer exposure times and a reasonable signal-to-noise ratio, about 120 to 1. A 200-ms delay before the start of the sampling period was introduced to eliminate vibration from the shutter system. The total image acquisition time was 1.3 s, unless otherwise stated.

Experiments with a Model System

A model system with a geometry and size comparable with that of single cells has been devised to determine experimental variables that might affect the rate and extent of photochemical reactions. Benzo(a)pyrene at concentrations ranging from 1.25 μM to 1.25 mM in mineral oil was emulsified in 4 vol of distilled H_2O containing 0.4% Na deoxycholate. Vigorous vortexing gave stable spherical droplets, ranging from 10 to 100 μM in diameter. A photomicrograph of a typical droplet is shown in Fig. 3 (top left image). The fluorescence intensity values are projected isometrically (21) on a pixel by pixel basis in Fig. 3 (bottom left). The concentration of benzo(a)pyrene in the aqueous phase surrounding the emulsion was calculated to be $\sim 10^{-12}$ to 10^{-13} M, based on the equilibrium distribution of 10^{-8} for benzo(a)pyrene between the aqueous phase and phospholipid (36). Therefore, the microscopic concentrations of benzo(a)pyrene were assumed to be those of the mineral oil solutions.

A 10-μl sample of the emulsion was placed on a 50 × 50-mm No. 1 microscope coverglass mounted in the Bionique chamber, covered with a 22 × 22-mm coverglass, and examined with the × 63, 1.4 NA objective. Rate constant measurements were made on various size areas in the object plane, ranging from a single pixel at the center of a droplet to an entire field containing several droplets. Rate constants from single pixel data were calculated from 512 time points, sampled over at least three halftimes of fluorescence photobleaching.

The time course of fluorescence decrease as a function of excitation intensity is shown in Fig. 3 (top right). The observed rate constants decreased proportionally with the attenuation of the excitation light. The halftime increased from 23 s at maximum illumination, to 120 s when the excitation light was decreased 95%. With low excitation intensities (<5% of the maximum intensity), the observed rate constants reached a limiting value with a halftime of ~3 min. The lower limit for the observed rate constant appeared to be due to the diffusion of benzo(a)pyrene into the area of measurement. To test this hypothesis, we photobleached a small area with the unattenuated beam, then observed the reappearance of fluorescence using an attenuated beam. The fluorescence increase followed a simple exponential with a halftime of 3 min. The

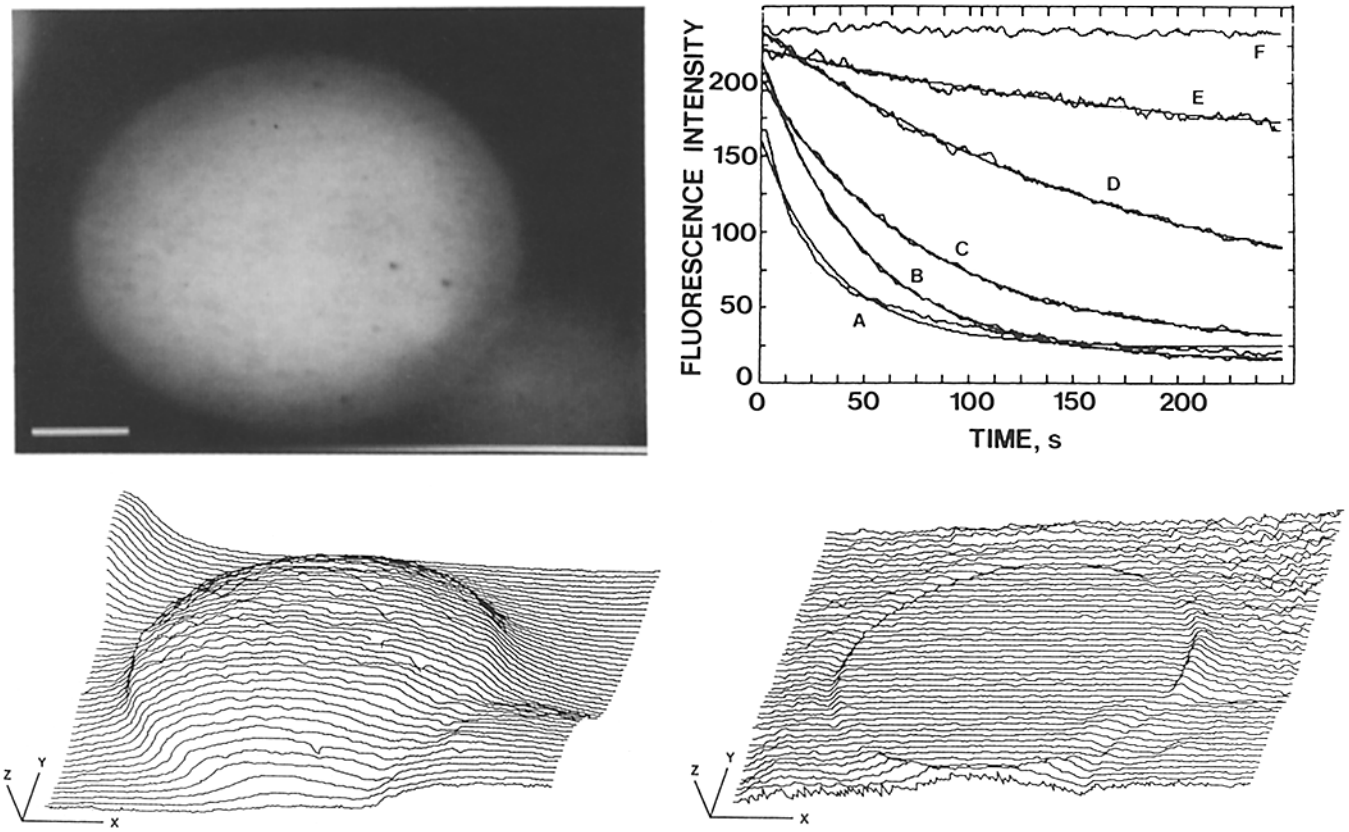

FIGURE 3 Effect of excitation light intensity and reducing conditions on photobleaching of benzo(a)pyrene in a mineral oil microemulsion. (*Top left*) Fluorescent image of a typical microemulsion containing 1.25 μM benzo(a)pyrene. (Bar, 10 μm.) (*Bottom left*) Isometric projection of the fluorescence intensity values for a microemulsion containing 1.25 μM benzo(a)pyrene. The scale of the *x*- and *y*-axes is 10 μm, and for the *z*-axis, 64 gray levels, 25% of full scale. (*Top right*) Decay curves of benzo(a)pyrene fluorescence in a series of microemulsions, 17–29-μm diameters, obtained under decreasing excitation light intensities. Each experimental curve is superimposed on the respective calculated exponential decay curve. For curve *A*, there was no attenuation of excitation light. For curves *B–E*, attenuation was 60, 80, 95, and 99%, respectively. Curve *F* was obtained with maximum excitation in the presence of 2 M $Na_2S_2O_5$. Halftimes for curves *A–E* were 23.6, 33.8, 53.3, 125.8, and 160.4 s, respectively. (*Bottom right*) Isometric projection of the rate constants within an individual vesicle, photobleached with full illumination. The absence of diffusion barriers allows the spatial uniformity of photobleaching in this system. A bivariate frequency histogram of the rate constants as a function of initial intensity revealed a gaussian distribution, ranging from 0.018 to 0.030 s^{-1}, with a mean of 0.025 s^{-1}. The scale of the *x*- and *y*-axes is 10 μm. For the *z*-axis, the scale is 0.016 s^{-1} to 0.032 s^{-1}.

observed photobleaching rate constants in this model system did not vary over three orders of magnitude of benzo(a)pyrene concentrations, indicating there was no significant concentration dependence. Similarly, no significant differences in rate constants, as a function of vesicle size, was observed if the entire vesicle was illuminated (Fig. 3, bottom right).

To remove molecular O_2 from the microemulsion dispersion, a 2-ml volume of a 2 M $Na_2S_2O_5$ was layered over the coverglass sandwich. After equilibration for 3–5 min, no loss of fluorescence intensity was observed with continuous maximum excitation over a period of 10 min, as shown by the top trace in Fig. 3 (top right). However, photobleaching did occur after 20 min exposure, presumably due to consumption of the reducing agent and diffusion of atmospheric O_2 into the sample.

Effects of Compartmentalization of Photobleaching

To investigate the spatial variation of photobleaching, an algorithm was developed that allowed determination of the rate constants, initial and final fluorescence intensities, and the corresponding standard deviations and correlation coefficients on a pixel-by-pixel basis for an image composed of 256 columns by 240 rows, or 61,440 pixels. The input data consists of 20 fluorescence images acquired at variable time intervals from samples under continuous illumination. With the present system, the minimum time interval is 5 s. Fig. 4 illustrates the data and the output from the program. Fig. 4 shows digital images of a human fibroblast at various times during a photobleach experiment. This cell was labeled with benzo(a)pyrene solubilized in LDL, as described in the figure legend. The calculated zero-time image, given by $A_{(x,y)} + B_{(x,y)}$, is shown in Fig. 4 (top right); the final image at infinite time, given by $A_{(x,y)}$, is shown in Fig. 4 (bottom right).

Fig. 5 illustrates the effect of increasing the illumination intensity on the rate constant maps of the photobleaching processes. These isometric plots, Fig. 5 (left top, center, and bottom), give the rates for 1%, 40%, and 100%, respectively, of the maximum intensity level. Although different cells were used for each experiment, the difference in the magnitude of the rate constants is apparent. The mean values from only intracellular areas for each excitation level were 0.0416 ± 0.005 for 32,101 pixels (no attenuation), 0.018 ± 0.004 for

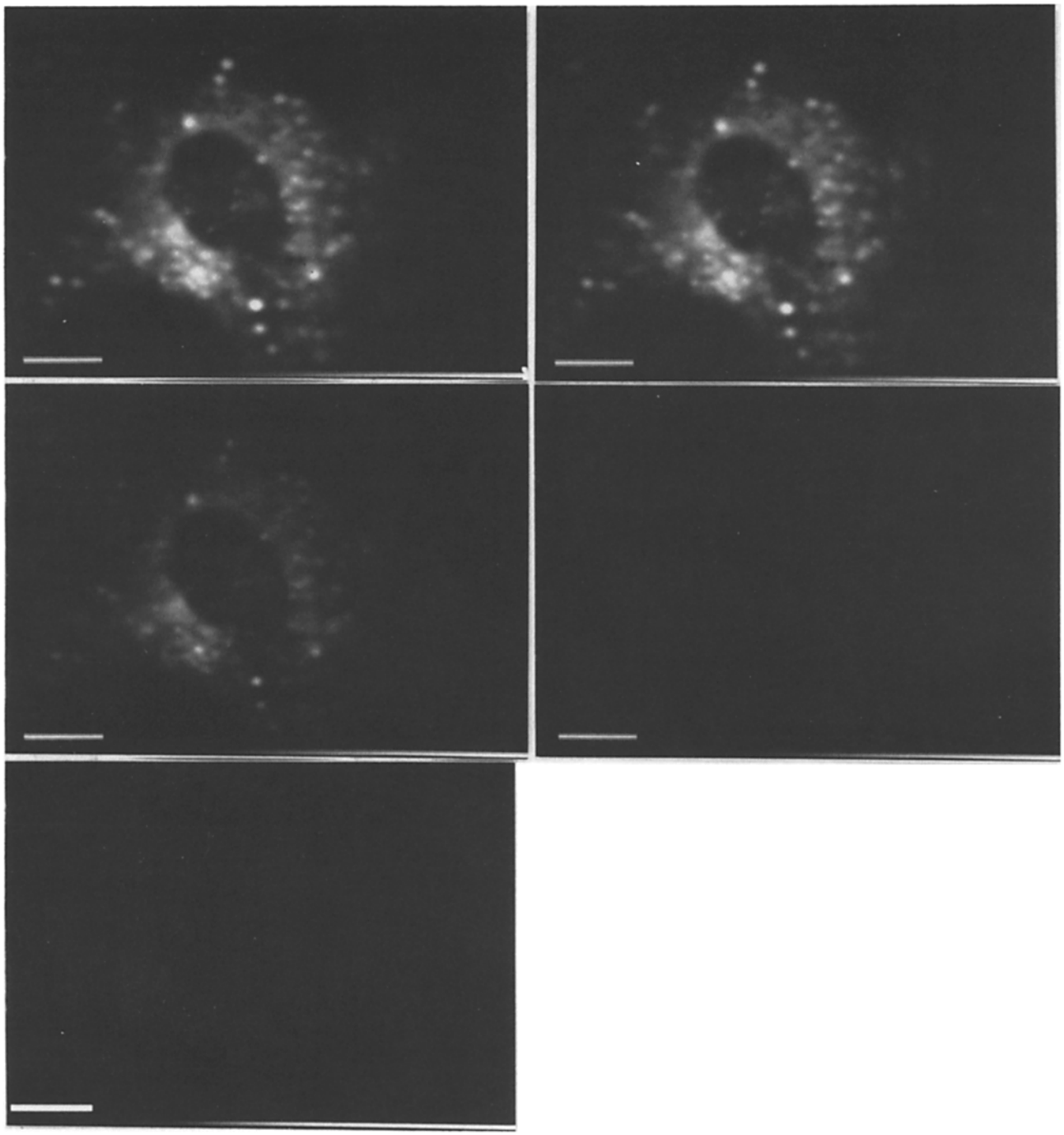

FIGURE 4 Benzo(a)pyrene photobleaching in fibroblasts. Human fibroblasts were fixed with 3% formaldehyde and incubated for 24 h with LDL containing 2 mol% benzo(a)pyrene at 50 μg of protein·ml^{-1}. (*Left images*) Images of benzo(a)pyrene excited with 100% of the maximum intensity for 1, 5, and 20 s, respectively. (*Right top image*) The initial image, calculated for zero time, given as $A_{(x,y)} + B_{(x,y)}$. (*Right bottom image*) The final image, calculated for infinite time, given as $A_{(x,y)}$. Bar, 10 μm.

21,026 pixels (40% attenuation), and 0.0007 ± 0.0006 for 16,878 pixels (99% attenuation). This comparison indicates that we are limited at these low illumination levels by the noise or dark current of the system. Attempts to use $Na_2S_2O_5$ to prevent photobleaching with live cells have been unsuccessful, in the sense that the cells are not viable, although the photobleach rates decreased as expected. The isometric plot of the standard deviations of the rate constant map is shown as Fig. 5 (top right). A rate constant map for photobleaching of benzo(a)pyrene, displayed as differences in gray level values, is shown as Fig. 5 (bottom right). The gray scale for the rate constant map ranges from 0 to 0.255 s^{-1}.

The localization and microenvironment of a probe within cells had a marked effect on photochemical processes. In our initial studies of these processes, we have used fluorescent probes that label both live and fixed cells. Acridine orange has been used to stain acidic compartments and nuclear regions, NBD-cholesterol to investigate membrane labeling and fluorescein isothiocyanate (FITC)-labeled antibodies to explore fixed material.

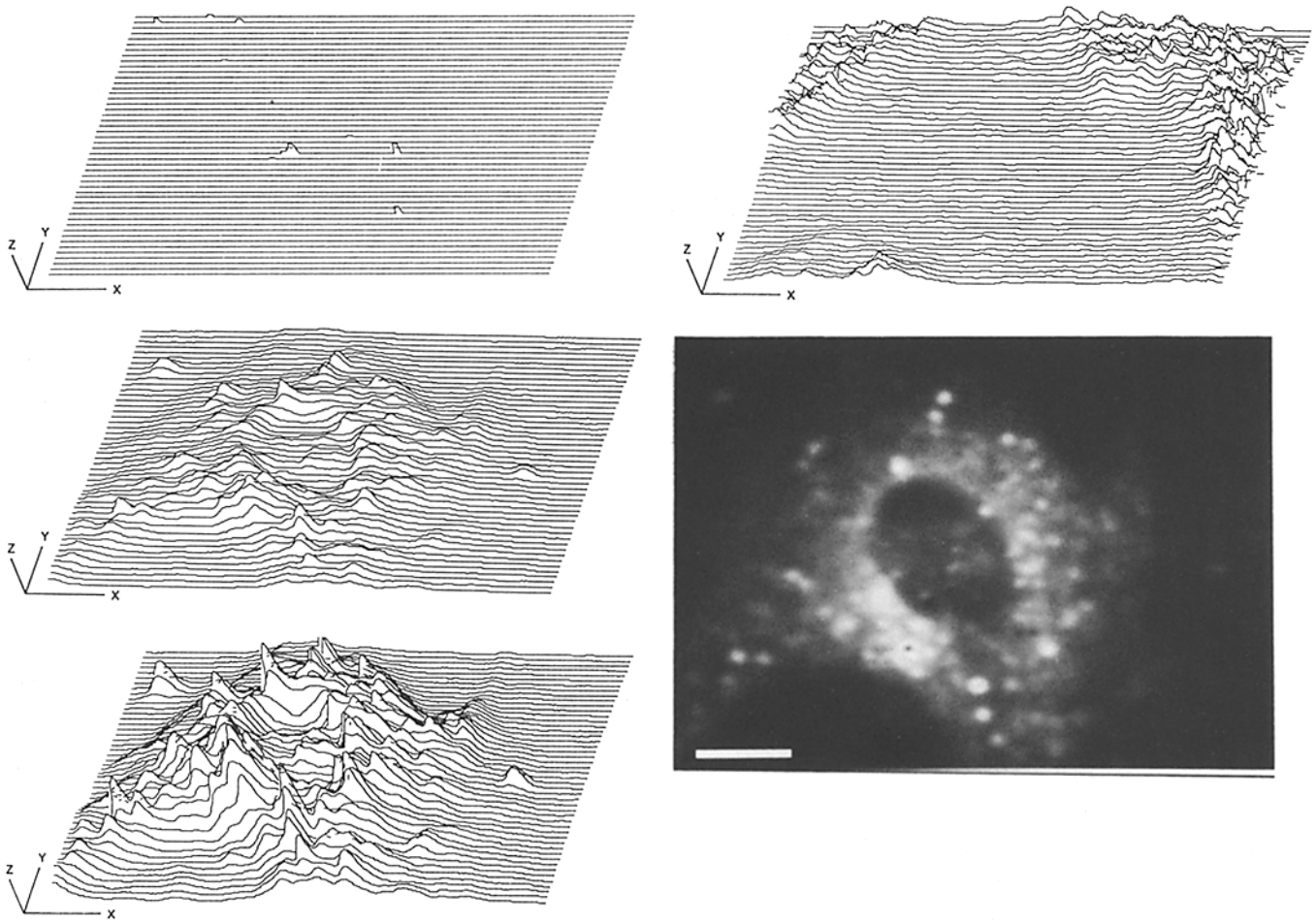

FIGURE 5 Isometric plots of photobleaching rate constant maps for benzo(a)pyrene in fibroblasts. (*Left panels*) Isometric plots of the calculated maps of the photobleaching rate constants, given as $k_{(x,y)}$. The excitation light was 1, 60, and 100% of the maximum intensity level, respectively. For all plots, the scale for the *x*- and *y*-axes is 10 μm and 0–0.032 s^{-1} for the *z*-axis. (*Right top*) Isometric plots of the standard deviations of the *left bottom* rate constant map displayed on the same scale. (*Right bottom*) Rate constant map of benzo(a)pyrene photobleaching. The gray scale for the values of rate constants was from 0 to 0.128 s^{-1}.

As shown in Fig. 6 for a primary rat hepatocyte, acridine orange–labeled nuclei, particularly nucleoli and acidic compartments. The left panels of Fig. 6 demonstrate the rapid photobleaching that occurred within 30 s. The brightest structures can be visualized at higher camera gains even after extensive photobleaching (top right image in Fig. 6, left). The graph in Fig. 6 (bottom right image in left panel) gives a more objective evaluation of the difference in photobleach rates between two small areas, one over an acidic compartment and the other over a nucleolus. The data were obtained by sampling each area at increasing times of illumination. The solid lines are those calculated from the three-parameter monoexponential fit software. The rate constant for the acidic compartment (○) was 0.048 s^{-1} and 0.154 s^{-1} for the nucleolus (x). The right panel of Fig. 6 (top left image) gives the rate constant map for the entire image. The range of photobleaching rates in this particular experiment was 0.031–0.194 s^{-1}. The bottom left image of the right panel of Fig. 6 is an isometric projection of the rate constant map.

To determine the consequences of these differential photobleach rates on the evaluation of fluorescence images obtained by the more conventional photographic image, we compared the zero-time image calculated from the three-parameter exponential fit with a "photograph" calculated by summing the intensities from the 20 images taken during the photobleaching experiment. The reasoning is that a photographic film would integrate the decreasing intensities for about the same time used to determine the photobleaching rates. These two images, the zero-time image and the "photograph," were compared by subtracting the "photograph" from the zero-time image. The isometric projection of the differences in intensity values is shown in the right panel of Fig. 6 (top right image). In this figure, a positive value indicates that the $A_{(x,y)} + B_{(x,y)}$ image, the calculated zero time image without photobleaching, was brighter or more intense than the "photograph," the integrated image. The results indicate that areas with the highest rate constants are significantly underrepresented in the photographic image, as much as 20-fold in some areas. This underrepresentation would be most acute in a "real" experiment, where it is necessary to locate and focus a given region before actually exposing the photographic emulsion.

Finally, we have observed that, with acridine orange, there may be multiple reactions and/or compartments within a cell. This is shown in the right panel of Fig. 6 (bottom right plot), which is an isometric projection of the plot of the rate con-

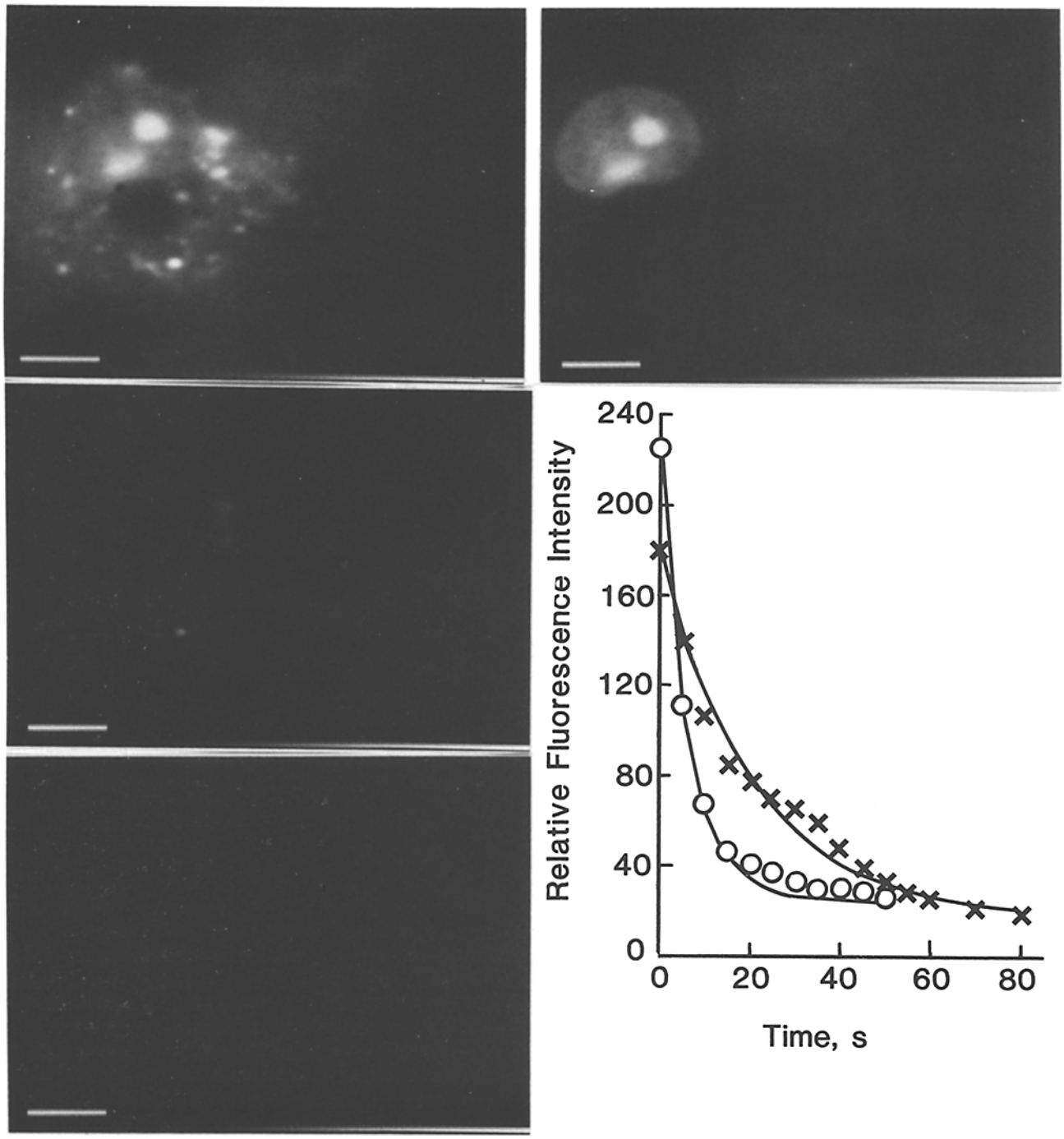

FIGURE 6 Photobleaching of acridine orange in hepatocytes. (*Left page*) (*left images*) Fluorescent images taken at 1, 10, and 30 s, respectively, under continuous excitation. Bar, 10 μm. (*Top right image*) Fluorescent image taken at 6.3 min, 3 min after termination of continuous excitation. The camera gain was increased 30-fold, compared with that for the left images. (*Bottom right*) Intensity values samples from two areas, 1 μm in diameter, over a nucleolus (O) and over an acidic compartment (x). Lines indicate a fit of a three-parameter monoexponential to the raw data. (*Right page*) (*top left image*) Rate constant map of the entire image, given as $k_{(x,y)}$. The gray scale for the values of rate constants ranges from 0 and 0.255 s^{-1}. The mean rate constant within the cell perimeter was 0.134 s^{-1}, with an intracellular range of 0.021–0.194 s^{-1}. (*Bottom left*) Isometric projection of the rate constant image. The scale for the *z*-axis is 0–0.064 s^{-1}, and 10 μm for the *x*- and *y*-axes. (*Top right*) Isometric projection of the difference in intensity values obtained by subtraction of the image obtained by integration of the 20 images acquired during the photobleaching time course from the calculated initial intensity image, as described in Materials and Methods. The scale for the *x*- and *y*-axes is 10 μm and 64 gray levels for the *z*-axis. (*Bottom right*) Isometric projection of the rate constants as a function of initial fluorescence intensity values. Calculated initial fluorescence intensity values are plotted on the *x*-axis, the values for the rate constants on the *y*-axis, and the frequency of pixels with given values for intensities (*x*) and rate constants (*y*) on the *z*-axis. The scale for the rate constants on the *y*-axis is 0.031–0.194 s^{-1}. For the initial intensity values on the *x*-axis, the scale is 0–255 gray levels. For the number of pixels at each location, the scale is 0–64 on the *z*-axis.

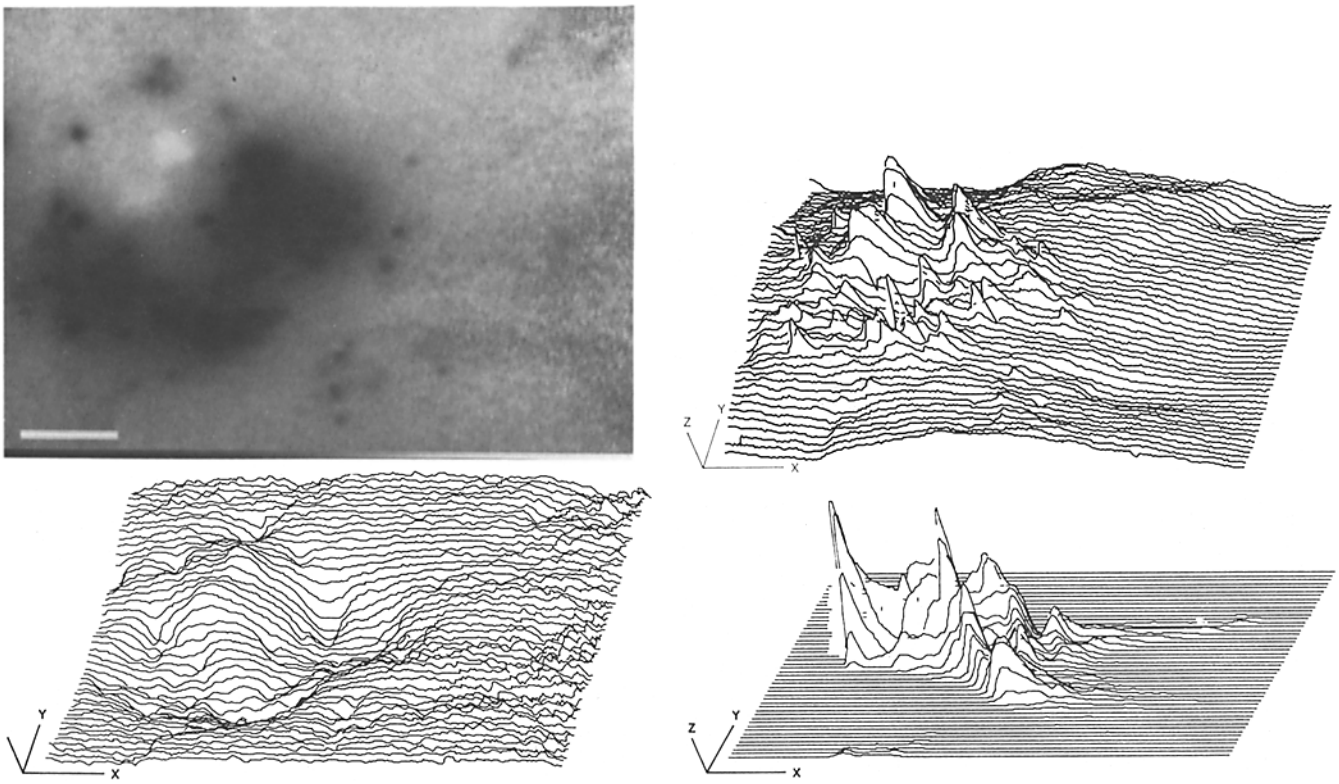

stants versus the initial fluorescence intensity. The histogram is complex, with many components of the photobleaching population.

Photobleaching of NBD-Cholesterol

We have used NBD-cholesterol as a probe of lipid environments in living cells. The microenvironments accessible to this probe generated marked differences in the rates of photobleaching. A result for human fibroblasts, loaded by incubation with 10 μM NBD-cholesterol in 100 μM 1-palmitoyl-2-oleoylphosphatidylcholine vesicles for 24 h at 37°, is shown in the left panel of Fig. 7. Images were taken at 1 and 100 s after exposure to excitation light, left top and bottom images, respectively. The calculated zero-time image and the final image at infinite time are shown as the right top and bottom images, respectively. The rate constant data are illustrated in the right panel of Fig. 7 as a gray scale image (top left image) and as an isometric projection of the data (bottom left plot). The differences in fluorescence intensities between the integrated "photograph" and the calculated zero-time image are shown as the top right plot in the right panel of Fig. 7. Positive values represent rapidly bleaching areas from which intensity information would be lost by recording the image using a photographic emulsion. The differences were 10-fold in some areas. Fig. 7, (bottom right plot) shows a bivariate frequency histogram of initial fluorescence intensity versus photobleaching rate constant on a pixel-by-pixel basis. This analysis shows a complex pattern, with at least two populations of values, arguing for the existence of different microenvironments that produce different photobleaching effects for this lipid probe.

Photobleaching of Fixed Cells Stained with Antibodies for Conventional Indirect Immunofluorescence

We have evaluated the photobleaching rates of cells fixed and stained by conventional procedures for indirect immunofluorescence. Fixed WI-38 fibroblasts were incubated with a murine monoclonal antibody to human platelet gelsolin to demonstrate stress fibers in these cells (37). FITC-conjugated goat anti-mouse IgG was then applied to the cells. Fig. 8 illustrates the results. Fig. 8 (top left image) is the calculated zero-time image and Fig. 8 (left upper center panel) is the final image at infinite time. The rate constant map and isometric projection of the rate constant map appear as the two lower left panels of Fig. 8. The difference between the calculated zero-time image and the integrated image is Fig. 8 (top right panel). The differences were as much as 17-fold in some areas. The distribution of photobleaching rate constants was heterogenous. The two principal components of the bivariate frequency histogram of initial intensity values versus observed rate constants are illustrated in Fig. 8 (right bottom panel). Each population of rate constants was associated with specific regions of the image. The locations of the rate constant cluster at the left end of the projection were located outside the cell boundaries, the white areas in the right upper center image. The rate constants for areas inside the cell, the white area in the right lower center image, range to the right end of the projection.

The photobleaching rate constants for several fluorophores, studied in microemulsions and in both fixed and living cells, are summarized in Table I. The values observed in single

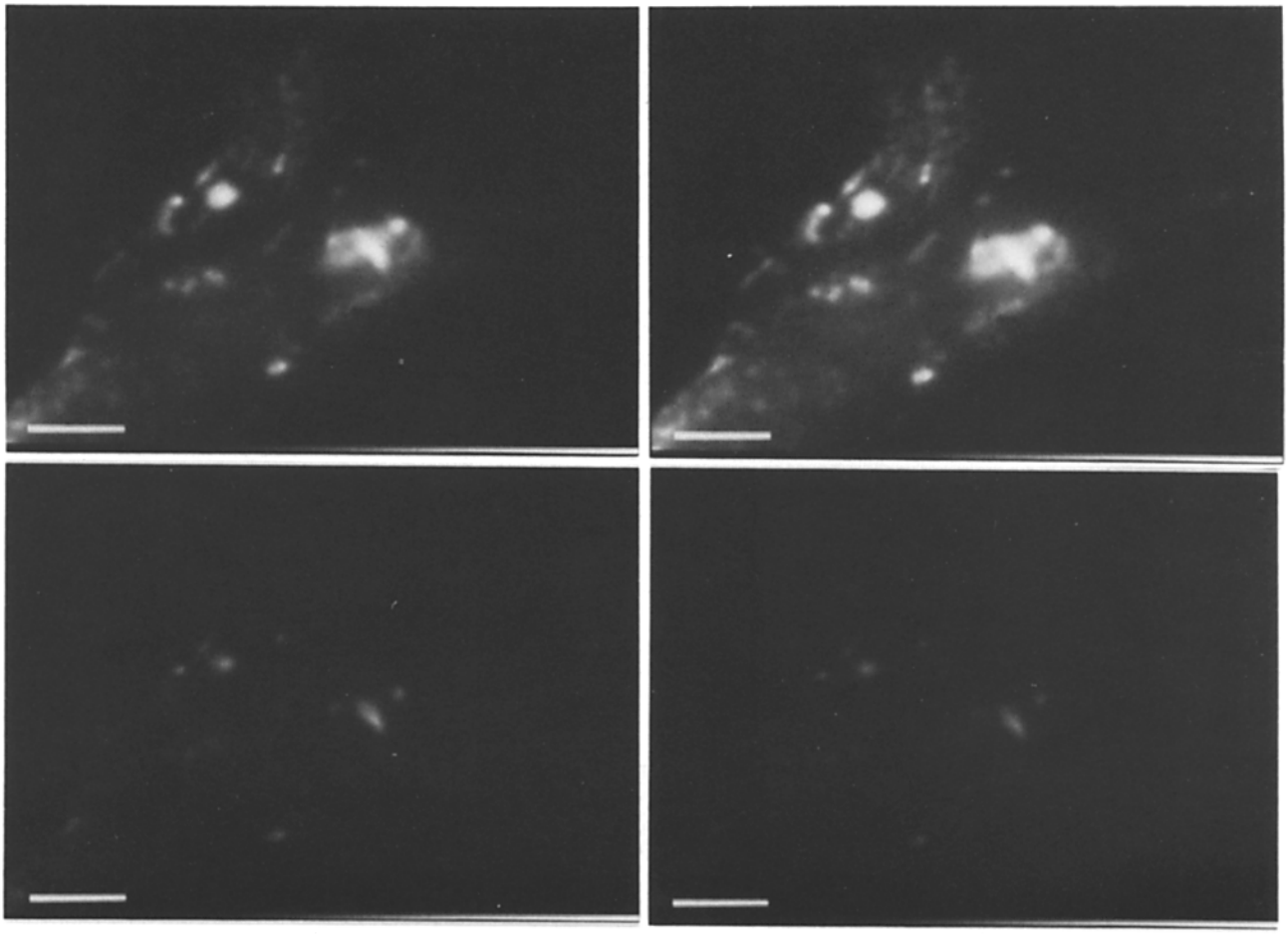

FIGURE 7 Photobleaching of NBD-cholesterol in human fibroblasts. Human fibroblasts were labeled with NBD-cholesterol in 1-palmitoyl-2-oleoylphosphatdylcholine vesicles as described in Materials and Methods. (*Left page*) (*left images*) Images taken at 1 and 100 s, respectively, of continuous exposure to maximum intensity excitation light. (*Right images*) Calculated initial and final intensity images, respectively. The zero-time image is given as $A_{(x,y)} + B_{(x,y)}$, and at infinite time, image is given as $A_{(x,y)}$. Bar, 10 μm. (*Right page*) (*left top image*) Rate constant map, given as $k_{(x,y)}$, with a range of 0–0.255 s^{-1}, full scale. (*Left bottom*) Isometric projection of the rate constant map. The scale for the *x*- and *y*-axes is 10 μm and 0–0.064 s^{-1} for the *z*-axis. (*Right top*) Isometric projection of the difference in intensity values obtained by subtraction of the image obtained by integration of the 20 images acquired during the photobleaching time course from the calculated initial intensity image, as described in Materials and Methods. The scale for the *x*- and *y*-axes is 10 μm and 64 gray levels for the *z*-axis. (*Right bottom*) Bivariate frequency histogram of rate constants as a function of initial fluorescence intensity values. The scale for the rate constant on the *y*-axis is 0–0.255 s^{-1}; for the initial intensity values on the *x*-axis is 0–255 gray levels; and for the number of pixels at each coordinate is 0–64 on the *z*-axis.

pixel samples occurred in punctate areas in the cells. The rate constants for individual cells were obtained by the following procedure. A spatial mask was defined with the appropriate phase image to include only areas within the perimeter of the cell. The corresponding rate constant map of only the intracellular area was then analyzed with this spatial mask. Presentation of the rate constant data as an average of the entire cell obscures the differences in photobleaching that can be appreciated only by a pixel-by-pixel comparison of rate constant values of the cellular maps. Data acquired by photomultipliers as sensing devices in microscopy systems appear to underestimate significantly the magnitude of photobleaching.

DISCUSSION

A detailed discussion of all the photochemical processes that lead to decreased fluorescence frequently observed during microscopic measurements is beyond the scope of this paper. These light-induced chemical reactions are mechanistically distinct from oxygen quenching of fluorescence described by Vaughn and Weber (38). This quenching is a reversible photophysical process that does not produce chemically modified ground state products. Unfortunately, the identification and quantification of the products of photodegradation processes occurring in specimens studied with a fluorescence microscope will be difficult, for two reasons. First, the observation of different rates of fluorescence decay suggests multiple reactions are occurring. Second, the extremely small amounts of material generated preclude most analytical methods.

Several studies have been concerned with the nature of these photoprocesses and the role of O_2. Oster et al. (39, 40) established that fluorescein and acridine act as photosensitizers in the oxidation of *p*-toluenediamine. This photochemical process was dependent on oxygen concentration, showing saturation above 20 μM or ~2% (vol/vol). Livingston and Owen (41) postulated that the long-lived triplet states ($\sim 10^{-4}$ s) that are quenched efficiently by O_2 react to generate per-

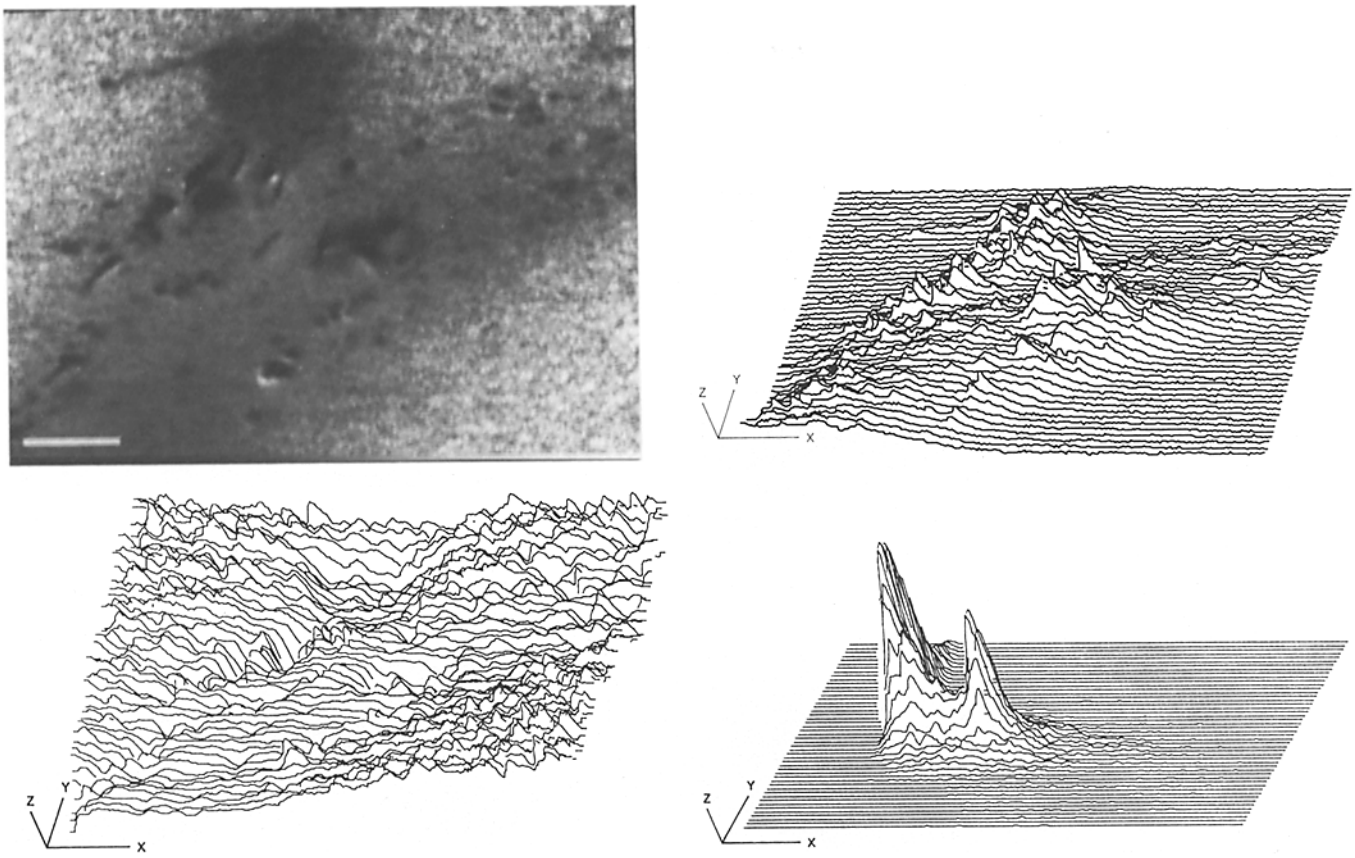

oxides which in turn oxidized the fluorophores. This proposal is supported by the observations of Lanni et al. (21) that there was no photobleaching of FITC-actin upon excitation by a milliwatt laser if the solutions are carefully deoxygenated. Khan and Kasha (42) have also shown that benzo(a)pyrene in organic solution generates singlet oxygen (O_2) when irradiated at 365 nm. This process appears to involve triplet state interactions. Johnson et al. (43), by contrast, report that oxygen does not significantly contribute to the photochemical degradation of FITC conjugates, although the actual oxygen concentrations of the solutions used in this study were not determined independently. In addition, the introduction of argon above the solutions is not an efficient method to deoxygenate aqueous solutions (44).

Other studies suggest that at least two mechanisms may be involved. In addition to interaction of molecular O_2 with triplet states to produce singlet oxygen, a second mechanism, the absorption by a triplet state of a second photon to produce a radical and a solvated electron (45), may be important in photosensitized reactions. This second mechanism would permit a fluorophore to be photodegraded in the absence of oxygen.

Irrespective of the exact nature of the photochemistry involved in the bleaching reactions, some objective means is necessary to study these processes and evaluate fluorescence images in a quantitative fashion. Our approach to this problem has been to develop a digital image processing system that incorporates a low light level camera to maximize the signal to noise ratio and to minimize illumination levels and exposure times. This strategy provides an objective means to compare video equipment and to maximize control of day-to-day variables such as lens alignment, lamp stability, and focus. Moreover, it furnishes a means to initiate the development of radiometric and geometric microscopic fluorescence standards and, finally, allows the application of a whole range of image processing and image analysis methodology (22–26, 46–50).

We have used this instrumentation to study the effects of photobleaching on fluorescence experiments and to evaluate the degree to which photobleaching complicates the interpretation of such experiments. In calibrating our instrument, we have used an Optoliner, a device manufactured by Optical Instruments Corporation, that projects a pattern of known intensity onto the target of the camera. By using neutral-density filters, which have been standardized by absorption spectrophotometry, the output from the Optoliner was attenuated in steps to determine and calibrate the camera response directly. We emphasize that "white light" was used in these experiments. We have not made any effort to determine the spectral sensitivity of the camera.

The frequency response of the camera was estimated by measuring the contrast transfer function. From Fig. 2, there is a 60% reduction in contrast, for the camera only, at 15.8 line pairs per millimeter on the target. Assuming that the transfer functions for the optical elements in the microscope are 1.0, this resolution at the specimen plane, using the × 63 objective and no ocular lens, would be 1.6 line pairs per micrometer. In a bright field image, this means we would have a 60% reduction of contrast when two black lines were spaced 0.6–0.7 μm from each other. We assume this resolution is valid for fluorescence images, in that comparable fluorescent resolution standards are not available.

The results for actual experiments show that the photobleaching reactions are first order or pseudo-first order, except

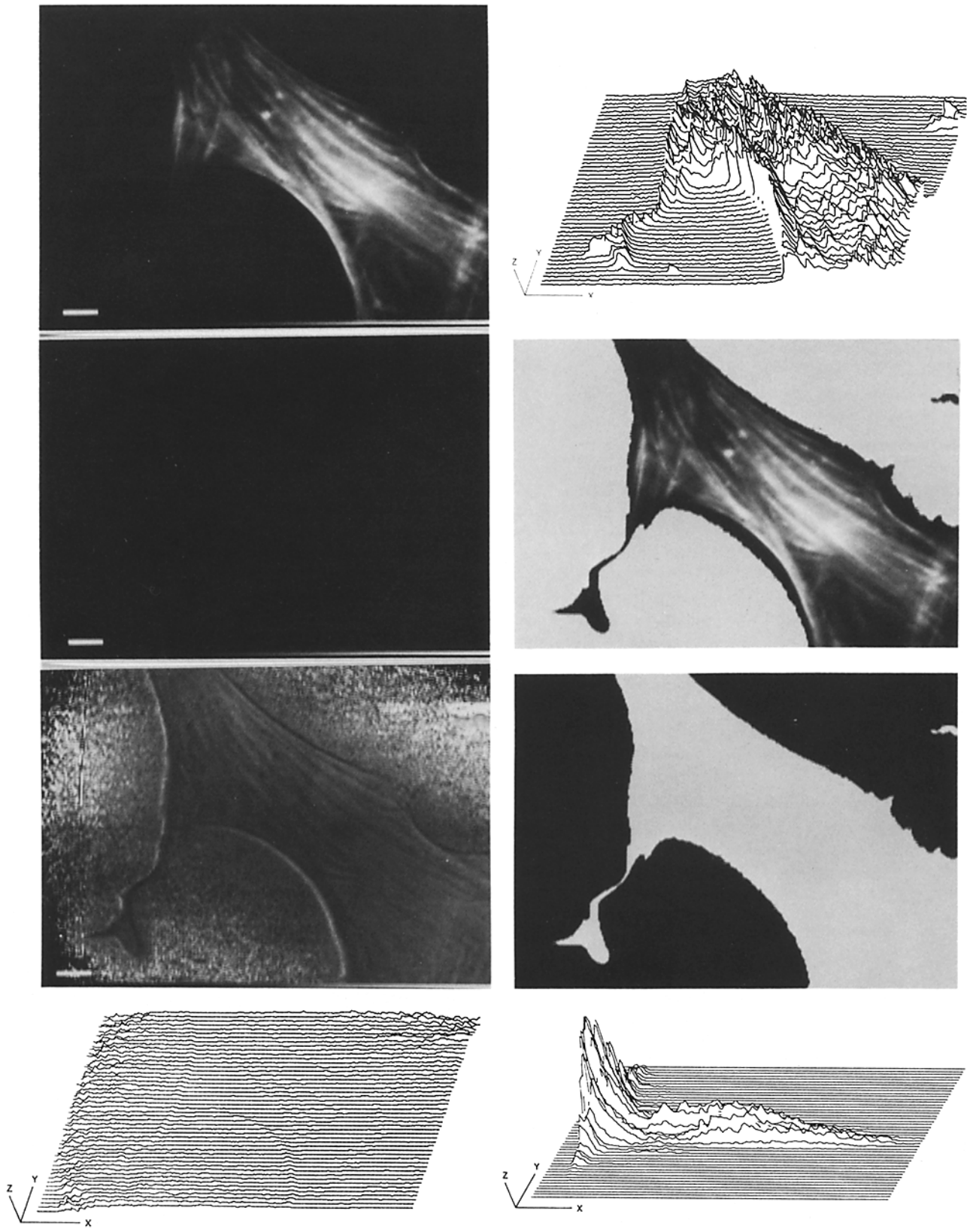
Z
Y
X
Z
Y
X
Z
Y
X

TABLE I

Photobleaching Rate Constants for Fluorophores

Fluorophore system	Single pixel rate constant	Intracellular rate constant
	s^{-1}	s^{-1}
Benzo(a)pyrene		
Cells	0.025 ± 0.002 (3)§	0.042 ± 0.006 (0.0–0.125)‖
Microemulsion	0.029 ± 0.007 (18)	0.025 ± 0.003 (0.018–0.030)
NBD-cholesterol		
Cells/LDL*	0.151 ± 0.05 (7)	
Cells/POPC*	0.141 ± 0.04 (9)	0.116 ± 0.019 (0.0–0.196)
Acridine orange		
Cells	0.048¶	0.134 ± 0.026 (0.03–0.194)
	0.154**	
Rhodamine-123		
Cells	0.069 ± 0.007 (5)	
FITC		
Cells‡	0.007 ± 0.003 (12)	0.012 ± 0.001 (0.009–0.021)
Tetramethylrhodamine isothiocyanine		
Cells‡	0.006 ± 0.002 (3)	
1,1′-Dioctadecyl-3,3,3′,3′,tetramethylindocarbocyanine		
Cells	0.003 ± 0.001 (5)	

* NBD-cholesterol was added as a component of LDL and 1-palmitoyl-2-oleoyl-phosphatidylcholine vesicles (POPC), respectively.
‡ Fibroblasts were fixed with 3% formaldehyde and permeabilized with 0.1% Triton X-100.
§ Number of experiments
‖ Range of rate constants within the cell perimeter.
¶ Acidic compartment from Fig. 6, lower right graph.
** Nucleolus from Fig. 6, lower right graph.

at the highest intensities where there is some indication from the decay curves that multiphoton processes may become more important (45). The observed rate constants over this range are linearly dependent upon the excitation energy. What was somewhat surprising is the clear observation that the rate constants for at least two environmentally sensitive probes are spatially heterogeneous. We originally observed variations in rate constants, determined on a limited number of pixels in different areas of a cell, and therefore implemented the algorithm to determine the three-parameter analysis for each pixel in the full image.

The origin(s) of the rate constant heterogeneity is unclear and will have to elucidated for each probe and for different cellular compartments. We suggest several possible origins for the differential photobleaching rates.

(*a*) Photophysical processes that affect quantum yield of the fluorophore are potentially important. Two examples seem likely. Certain fluorophores may partition into a specific compartment and reach sufficiently high concentrations to self-quench, or may have a high local concentration of quenching molecule(s).

(*b*) A particular compartment may contain molecules, such as cytochromes or pigments, that absorb at the excitation wavelength sufficiently to decrease the observed rate constant due to inner filter effects.

(*c*) There may be a high local concentration of one of the reactants for the photochemical processes. This seems particularly likely for O_2, which can reach high concentrations in lipid environments.

Which, if any, of these possibilities gives rise to the heterogeneity observed with NBD-cholesterol and acridine orange is not yet clear, although we suspect that concentration quenching may be important (51, 52).

One important finding for quantitative fluorescence measurements that emerges from the exponential fit data is the necessity to recognize and make the appropriate corrections for differences in photobleaching rates. We have illustrated this point by calculating the zero-time image and then comparing this image with a "photograph" obtained by summing images. The differences are significant and demonstrate that

FIGURE 8 Photobleaching of FITC-IgG in WI-38 fibroblasts. Fixed and permeabilized WI-38 fibroblasts were labeled initially with a murine monoclonal antibody to gelsolin and then with goat anti-mouse FITC-conjugated IgG. (*Left top and upper center images*) Calculated initial and final intensity images, respectively. The zero-time image is given as $A_{(x,y)} + B_{(x,y)}$, and infinite-time image is given as $A_{(x,y)}$. (*Left lower center image*) Rate constant map, given as $k_{(x,y)}$, with a range of 0–0.025 s^{-1}, full scale. Within the cell, the mean value for $k_{(x,y)}$ was 0.012 ± 0.0016. Bar, 20 μm. (*Left bottom*) Isometric projection of the rate constant map. Scales for the *x*- and *y*-axis are 20 μm, and 0.064 s^{-1} for the *x*-axis. (*Right top*) Isometric projection of the difference in intensity values obtained by subtraction of the image obtained by integration of the 20 images acquired during the photobleaching time course from the calculated initial intensity image. The scale of the *x*- and *y*-axes is 20 μm and 64 gray levels for the *z*-axis. (*Right upper center image*) The extracellular areas of the image are shown as the white areas. (*Right lower center image*) The intracellular areas of the image are shown in white. (*Right bottom*) Bivariate frequency histogram of rate constants as a function of initial fluorescence intensity values. The component of the histogram to the left end of the plot is shown as the white extracellular regions in the right upper center image above. The low broad component to the right end of the plot is shown as the white intracellular area in the right lower center image. The scale for the rate constant on the *y*-axis is 0–0.025 s^{-1}. For the initial intensity values on the *x*-axis, the scale is 0–255 gray levels. For the number of pixels at each coordinate, the scale is 0–64 on the *z*-axis.

rapidly photobleaching components are underrepresented in the summed image. The observation argues that fluorescence quantification schemes based on conventional photography and subsequent densitometry will not prove to be useful. The heterogeneity of these photochemical reactions suggests that attempts to quantify fluorescence intensities by extrapolation, assuming there is only a single rate constant, back to initial intensity distributions may also be hazardous.

Finally, the results of this study also argue that it will be necessary to account for photobleaching in any serious attempts to measure fluorescence, either qualitatively or quantitatively, with a microscope. This may be done in fixed material by deoxygenating the mounting medium or by using free radical scavengers (53, 54). The problem of photobleaching will be more acute in living cells, where the only clear strategy appears to be a reduction in the intensity of excitation illumination to tolerable levels, in combination with quantification of the rates of photobleaching based on the methods developed in this study. This analytic approach is particularly important in experiments in which multiple fluorophores are used to obtain ratios of intensity values, where the differences in photobleach rates between the probes will cause significant error.

We thank Dr. Bette C. Sherrill for her generous gifts of primary cultures of rat hepatocytes and Dr. D. P. McNair for his efforts in characterizing the electronics in the image processor and the camera.

This work was supported by grants from the Gulf Oil Foundation, and the Robert A. Welch Foundation (Q-343), grants HL-15648, HL-23741, CA-31513, GM-26091, and GM-27468 from the U. S. Public Health Service, and grant R80-8773 from the Environmental Protection Agency. Additional funding was provided by Baylor College of Medicine. The Environmental Protection Agency does not necessarily endorse any commercial products used in this study. The conclusions represent the reviews of the authors and do not necessarily represent the opinions, policies, or recommendations of the Environmental Protection Agency. Dr. Plant was a predoctoral fellow (HL-07282) and Dr. Benson is a postdoctoral fellow (CA-07090), both supported by the U. S. Public Health Service.

Received for publication 18 June 1984, and in revised form 13 December 1984.

REFERENCES

1. Robbins, E., P. I. Marcus, and N. K. Gonatas. 1964. Dynamics of acridine orange-cell interactions; II. Dye-induced ultrastructural changes in multivesicular bodies (acridine-orange particles). *J. Cell Biol.* 21:49–62.
2. Johnson, L. V., M. L. Walsh, B. J. Bockus, and L. Bo Chen. 1981. Monitoring of relative mitochondrial membrane potential in living cells by fluorescence microscopy. *J. Cell Biol.* 88:526–535.
3. Hawkes, S. P., and J. C. Bartholomew. 1977. Quantitative determination of transformed cells in a mixed population by simultaneous fluorescence analysis of cell surface and DNA in individual cells. *Proc. Natl. Acad. Sci. USA.* 74:1626–1630.
4. Arndt-Jovin, D. J., and T. M. Jovin. 1977. Analysis and sorting of living cells according to deoxyribonucleic acid content. *J. Histochem. Cytochem.* 25:585–589.
5. Lemke, P. A., B. Kugelman, H. Morimoto, E. C. Jacobs, and J. R. Ellison. 1978. Fluorescent staining of fungal nuclei with a benzimidazol derivative. *J. Cell Sci.* 29:77–84.
6. Willingham, M. C., and I. Pastan. 1978. The visualization of fluorescent proteins in living cells by video intensification microscopy (VIM). *Cell* 13:501–507.
7. Taylor, D. L., and Y.-L. Wang. 1980. Fluorescently labelled molecules as probes of the structure and function of living cells. *Nature (Lond.)* 284:405–410.
8. Sengbusch, G., and A. A. Thaer. 1973. Some aspects of instrumentation and methods as applied to fluorometry at the microscale. *In* Quantitative Fluorescence Techniques as Applied to Cell Biology. A. A. Thaer and M. Sernetz, editors. Springer-Verlag, New York. 31–39.
9. Kerker, M., M. A. Van Dilla, A. Brunsting, J. P. Kratohvil, P. Hsu, D. S. Wang, J. W. Gray, and R. G. Langlois. 1982. Is the central dogma of flow cytometry true: that fluorescence intensity is proportional to cellular dye content? *Cytometry.* 3:71–78.
10. Kohen, E., and C. Kohen. 1977. Rapid automated multichannel microspectrofluorometry: a new method for studies on the cell-to-cell transfer of molecules. *Exp. Cell Res.* 107:261–268.
11. Kohen, E., C. Kohen, J. G. Hirschberg, A. Wouters, and B. Thorell. 1978. Multisite topographic microfluorometry of intracellular and exogenous fluorochromes. *Photochem. Photobiol.* 27:259–268.
12. Kohen, E., C. Kohen, B. Thorell, and B. Bartick. 1979. A topographic analysis of metabolic pathways in single living cells by multisite microfluorometry. *Exp. Cell Res.* 119:23–30.
13. Salmon, J.-M., E. Kohen, P. Viallet, J. G. Hirschberg, A. W. Wouter, C. Kohen, and B. Thorell. 1982. Microspectrofluorometric approach to the study of free/bound NAD(P)H ratio as metabolic indicator in various cell types. *Photochem. Photobiol.* 36:585–593.
14. Benson, D. M., J. A. Knopp, and I. S. Longmuir. 1980. Intracellular oxygen measurements of mouse liver cells using quantitative fluorescence video microscopy. *Biochim. Biophys. Acta.* 591:187–197.
15. Podgorski, G. T., I. S. Longmuir, J. A. Knopp, and D. B. Benson. 1981. Use of an encapsulated fluorescent probe to measure intracellular Po_2. *J. Cell. Physiol.* 107:329–334.
16. Ohkuma, S., and B. Poole. 1978. Fluorescence probe measurement of the intralysosomal pH in living cells and the perturbation of pH by various agents. *Proc. Natl. Acad. Sci. USA.* 75:3327–3331.
17. Tanasugarn, L., P. McNeil, G. T. Reynolds, and D. Lansing Taylor. 1984. Microspectrofluorometry by digital image processing: measurement of cytoplasmic pH. *J. Cell Biol.* 98:717–724.
18. Axelrod, D., D. E. Koppel, J. Schlessinger, E. Elson, and W. W. Webb. 1976. Mobility measurement by analysis of fluorescence photobleaching recovery kinetics. *Biophys. J.* 16:1055–1069.
19. Wolf, D. E., M. Edidin, and P. R. Dragsten. 1980. Effect of bleaching light on measurements of lateral diffusion in cell membranes by the fluorescence photobleaching recovery method. *Proc. Natl. Acad. Sci. USA.* 77:2043–2045.
20. Peters, R., A. Brunger, and K. Schulten. 1981. Continuous fluorescence microphotolysis: a sensitive method for study of diffusion processes in single cells. *Proc. Natl. Acad. Sci. USA.* 78:962–966.
21. Lanni, F., D. L. Taylor, and B. R. Ware. 1983. Fluorescence photobleaching recovery in solutions of labeled actin. *Biophys. J.* 8:351–364.
22. Berns, M. W., J. Edwards, K. Strahs, J. Girton, P. McNeill, J. B. Rattner, M. Kitzes, M. Hammer-Wilson, L.-H. Liaw, A. Siemens, M. Koonce, S. Peterson, S. Brenner, J. Burt, R. Walter, P. J. Bryant, D. van Dyk, J. Coulombe, T. Cahill, and G. S. Berns. 1981. Laser microsurgery in cell and developmental biology. *Science (Wash. DC.)* 213:505–513.
23. Walter, R. J., and M. W. Berns. 1981. Computer-enhanced video microscopy: digitally processed microscope images can be produced in real time. *Proc. Natl. Acad. Sci. USA.* 78:6927–6931.
24. Stoward, P. J., and J. S. Ploem. 1982. The histochemical basis of quantitative histology. *J. Microsc. (Oxf.)* 128:49–56.
25. Berns, G. S., and M. W. Berns. 1982. Computer-based tracking of living cells. *Exp. Cell Res.* 142:103–109.
26. Berns, M. W., and R. J. Walter. 1982. Laser microirradiation and computer video optical microscopy in cell analysis. *Cell Anal.* 1:33–54.
27. Evans, M., P. J. A. Davies, and M. Costa. 1982. Video time-lapse microscopy of phagocytosis and intracellular fate of crystalline nickel sulfide particles in cultured mammalian cells. *Cancer Res.* 42:2729–2735.
28. Martin, P. M., H. P. Magdelenat, B. Benyahia, O. Rigaud, and J. A. Katzenellenbogen. 1983. New approach for visualizing estrogen receptors in target cells using inherently fluorescent ligands and image intensification. *Cancer Res.* 43:4956–4955.
29. Castleman, K. R. 1979. Digital Image Processing. Prentice-Hall, Inc., Englewood Cliffs, NJ. 429 pp.
30. Newnan, W. M., and R. F. Sproull. 1979. Principles of Interactive Computer Graphics. 2nd edition. McGraw-Hill Book Co., New York. 541 pp.
31. Wentworth, W. E. 1965. Rigorous least squares adjustment. Application to some non-linear equations, I. *J. Chem. Educ.* 42:96–103.
32. Plant, A. L., D. M. Benson, and L. C. Smith. 1985. Cellular uptake and localization of carcinogenic polycyclic aromatic hydrocarbons by digital fluorescence imaging microscopy. *J. Cell Biol.* 100:1295–1308.
33. Craig, I. F., D. P. Via, W. W. Mantulin, H. J. Pownall, A. M. Gotto, Jr., and L. C. Smith. 1981. Lipoproteins reconstituted with steroids containing the nitrobenzoxadiazole fluorophore. *J. Lipid Res.* 22:687–696.
34. McCord, T. B., J. P. Bosel, and M. J. Frankston. 1975. Performance of the MIT silicon vidicon imaging system at the telescope. *In* Image Processing Techniques in Astronomy, V. deJager and F. Nieuwenhuijzen, editors. D. Reidel Publishing Co., Dordrecht, Holland. 91–96.
35. Wrigley, N. G., R. K. Chillingworth, E. Brown, and A. N. Barrett. 1982. Multiple image integration: a new method in electron microscopy. *J. Microsc. (Oxf.).* 127:201–208.
36. Doody, M. C., H. J. Pownall, Y. J. Kao, and L. C. Smith. 1980. Kinetics and mechanism of transfer of fluorescent fatty acid between single bilayer phospholipid vesicles. *Biochemistry.* 19:108–116.
37. Hwo, S., M. C. Kurth, J. Dingus, C. Carron, I. Meza, and J. Bryan. 1983. The localization of gelsolin using monoclonal antibodies against the human platelet protein. *J. Cell Biol.* 97(2, Pt.2):281a. (Abstr.)
38. Vaughan, W., and G. Weber. 1970. Oxygen quenching of pyrene-butyric acid fluorescence in water. A dynamic probe of the microenvironment. *Biochemistry.* 9:464–473.
39. Oster, G., and A. H. Adelman. 1956. Long-lived states in photochemical reactions. I. Photoreduction of eosin. *J. Am. Chem. Soc.* 78:913–916.
40. Oster, G., J. S. Bellin, R. W. Kimball, and M. E. Schrader. 1959. Dye sensitized photooxidation. *J. Am. Chem. Soc.* 81:5095–5099.
41. Livingston, R., and K. E. Owens. 1956. A Diffusion-controlled step in chlorophyll-sensitized photochemical autooxidations. *J. Am. Chem. Soc.* 78:3301–3305.
42. Khan, A. U., and M. Kasha. 1979. Direct spectroscopic observation of singlet oxygen emission as 1268 nm excited by sensitizing dyes of biological interest in liquid solution. *Proc. Natl. Acad. Sci. USA.* 76:6047–6049.
43. Johnson, G. D., R. S. Davidson, K. C. McNamee, G. Russell, D. Goodwin, and E. J. Holborow. 1982. Fading of immunofluorescence during microscopy: a study of the phenomenon and its remedy. *J. Immunol. Methods.* 55:231–242.
44. Rollie, M. E., C.-N. Ho, and I. M. Warner. 1983. Sample deoxygenation for fluorescence spectrometry by chemical scavenging. *Anal. Chem.* 55:2445–2448.
45. Calmettes, P. P., and M. W. Berns. 1983. Laser-induced multiphoton processes in living cells. *Proc. Natl. Acad. Sci. USA.* 80:7197–7199.
46. Wied, G. L., P. H. Bartels, H. E. Dytch, F. T. Pishotta, and M. Bibbo. 1982. Rapid high-resolution cytometry. *Anal. Quant. Cytol.* 4:257–262.
47. Bartels, P. H., and G. B. Olson. 1980. Computer analysis of lymphocyte images. *In* Methods of Cell Separation. N. Catsimpoolas, editor. Plenum Press, New York and

Longon. 1–99.
48. Bradbury, S. 1983. Commercial image analysers and the characterization of microscopical images. *J. Microsc. (Oxf.)* 131:203–210.
49. Roos, K. P., and A. J. Brady. 1982. Individual sarcomere length determination from isolated cardiac cells using high-resolution optical microscopy and digital image processing. *Biophys. J.* 40:233–244.
50. Tanke, H. J., M. J. Van Driel-Kulker, C. J. Cornelisse, and J. S. Ploem. 1983. Combined flow cytometry and image cytometry of the same cytological sample. *J. Microsc. (Oxf.)* 130:11–22.
51. Hirschfeld, T. 1976. Quantum efficiency independence of the time integrated emission from a fluorescent molecule. *Appl. Opt.* 15:3135–3139.
52. Packard, B. S., K. K. Karukstis, and M. P. Klein. 1984. Intracellular dye heterogeneity determined by fluorescence lifetimes. *Biochim. Biophys. Acta.* 769:201–208.
53. Giloh, H., and J. W. Sedat. 1982. Fluorescence microscopy: reduced photobleaching of rhodamine and fluorescein protein conjugates by *n*-propyl gallate. *Science (Wash. DC.)* 217:1252–1255.
54. Platt, J. L., and A. F. Michael. 1983. Retardation of fading and enhancement of intensity of immunofluorescence by *p*-phenylenediamine. *J. Histochem. Cytochem.* 31:840–842.